Optical and Quantum Electronics (2023) 55:475
https://doi.org/10.1007/s11082-023-04734-8

# Evaluation of a proposed barium di-silicide tandem solar cell using TCAD numerical simulation

**M. Okil[1] · Ahmed Shaker[2] · Ibrahim S. Ahmed[1] · Tarek M. Abdolkader[1] · Marwa S. Salem[3,4]**

Received: 12 August 2022 / Accepted: 1 March 2023 / Published online: 3 April 2023


## Abstract

Barium di-silicide ($BaSi_2$) material has attracted noteworthy interest in photovoltaics, thanks to its stability, abundant nature, and excellent production feasibility. In this current work, a two-terminal (2T) monolithic all-$BaSi_2$ tandem solar cell is proposed and explored through extensive TCAD simulation. A $BaSi_2$ bottom sub-cell with a bandgap of 1.3 eV, and a $Ba(C_xSi_{1-x})_2$ top sub-cell with a tunable bandgap are employed in the design. It was found that a bandgap of 1.8 eV, which corresponds to $x = 0.78$, is the optimum choice to obtain the maximum initial power conversion efficiency ($\eta$) of 30%. Then, the tandem performance is optimized by investigating the impact of doping and the thickness of both absorber layers. Further, the current matching point is monitored whilst altering the thickness of the top cell resulting in $\eta = 32.83\%\%$, and a short-circuit current density ($J_{sc}$) of 16.47 mA/cm$^2$. Additionally, we have explored the influence of the defect density in the absorbers, and the work function of contacts on the performance parameters. All TCAD simulations are accomplished using the Silvaco Atlas package under AM1.5G illumination.

**Keywords** Tandem solar cell · Barium di-silicide · Current matching · TCAD simulation · Power conversion efficiency

✉ Ahmed Shaker
ahmed.shaker@eng.asu.edu.eg

[1] Department of Basic Engineering Sciences, Benha Faculty of Engineering, Benha University, Benha, Egypt

[2] Department of Engineering Physics and Mathematics, Faculty of Engineering, Ain Shams University, Cairo, Egypt

[3] Department of Computer Engineering, College of Computer Science and Engineering, University of Ha'il, Ha'il, Saudi Arabia

[4] Department of Electrical Communication and Electronics Systems Engineering, Faculty of Engineering, Modern Science and Arts University (MSA), Cairo, Egypt

## 1 Introduction

A photovoltaic solar cell has received much attention as an essential device for generating electricity. In this context, crystalline silicon is the highly commonly used material, accounting for more than 90% of installed solar cells (Pathi et al. 2017; Okil et al. 2021). Recently, Yoshikawa et al. have recorded a c-Si solar cell efficiency ($\eta$) of more than 26% (Green et al. 2022) which is near its theoretical efficiency limit of 29.56% (Schafer and Brendel 2018). However, the bandgap ($E_g$) of crystalline silicon is 1.12 eV, which is less than the optimal $E_g$ (1.35 eV) preferred for single-junction cell applications (Shockley and Queisser 1961). To attain higher efficiencies while keeping a relatively low cost, several thin-film solar cell (TFSC) materials, like Cu(In, Ga)$Se_2$, CdTe, and perovskite (Huang 2020; Gamal et al. 2021; Farooq et al. 2021), have drawn interest due to their greater optical absorption coefficient ($\alpha$) and larger $E_g$ compared with crystalline silicon. Still, several of the mentioned materials include toxic and/or rare elements.

Notably, an ultimate alternate absorbing material ought to have a high $\alpha$, high minority-carrier lifetime, and suitable bandgap for use as a single junction or in tandem cells. These characteristics are shared by orthorhombic barium di-silicide, which is stable, environmentally friendly, and has abundant constituent elements (Suemasu and Usami 2017). $BaSi_2$ has a 1.3 eV bandgap, and its $\alpha$ value is $3\times10^4$ $cm^{-1}$ at 1.5 eV (Toh et al. 2011), almost forty times that of crystalline silicon, regardless of the indirect bandgap of $BaSi_2$ (Kumar et al. 2014). The undoped $BaSi_2$ is an n-type semiconductor that has an approximate electron density of about $5\times10^{15}$ $cm^{-3}$ (Khan et al. 2012), roughly 10 µm minority-carrier diffusion length (Baba et al. 2012), and about 10 µs minority-carrier lifetime (Hara et al. 2013) that is appropriate for TFSC applications. Due to the reported values of $L$ and $\alpha$, an efficiency that is higher than 25% could be estimated from the $BaSi_2$ p–n junction diode having a thickness of 2 µm (Suemasu and Usami 2017). An efficiency of 23.17% has been achieved from p-type $Zn_3P_2$/n-type $BaSi_2$ heterojunction thin-film cell (Takahashi et al. 2017). In 2018, Tian et al. (2018) fabricated polycrystalline $BaSi_2$ thin films via an industrially applicable sputtering process and uncovered the process of structure transformation. Recently, Tian et al. (2020) deposited a Si/$BaSi_2$/Si heterostructure by magnetron sputtering with different Si layer thicknesses and it was found that the thickness of the Si layer has a great effect on oxide layer growth, Ba depletion, and multiphase Si layer formation at the heterojunction interfaces. These findings contribute to the development of $BaSi_2$/Si heterojunction solar cells and may allow the introduction of $BaSi_2$ to be used in conjunction with other materials thanks to the progress in material quality.

Notably, a conventional single-junction cell has some drawbacks, including thermalization and sub-bandgap losses. On the other hand, tandem solar cells have theoretically attained an efficiency greater than the S–Q limit by a combination of a wide bandgap top sub-cell along with a lower bandgap bottom sub-cell (Zhang et al. 2014). In this regard, the resultant tandem cells can be divided into several architectures based on their electrical connections and fabrication techniques (Werner et al. 2018; Wang et al. 2019). These include 2T, 3T and 4T tandem structures. The two sub-cells of the 2T monolithic solar cells are electrically coupled by a recombination film; thus, the current flowing into the two sub-cells is the same. Also, the open circuit voltage is given by the sum of the two sub-cells' open circuit voltages of this series connection. To increase the viability of $BaSi_2$ to be used in tandem cells, bandgap engineering should be performed to increase the $E_g$ from its initial value of 1.3 eV. By substituting part of Ba with Sr atoms to create $Ba_{1-x}Sr_xSi_2$, the $E_g$ of the compound can be adjusted to 1.4 eV (Morita et al. 2007). In the meantime, when

replacing some Si atoms with isoelectric C, the corresponding bandgap of $Ba(C_xSi_{1-x})_2$ can steadily increase from 1.3 to 3 eV (Imai and Watanabe 2010). Eventually, $BaSi_2$-based TSCs have been demonstrated in association with perovskite and crystalline silicon (Vismara et al. 2016; Tianguo 2019).

In this paper, we investigate a 2T monolithic tandem cell comprising barium di-silicide materials in the top cell as well as the bottom cell. Devices based on barium di-silicide material are regarded as environmentally friendly solar cells besides their low processing cost. A wide bandgap absorber layer is crucial for the top cell to permit a part of visible light and the near-infrared to pass through it and be readily absorbed by the bottom one. Thus, the presented designed TSC is based on combining $BaSi_2$ (1.3 eV) and $Ba(C_xSi_{1-x})_2$ (1.6–1.9 eV) materials for the bottom and top sub-cells, respectively (Imai and Watanabe 2010; Eperon et al. 2017). Firstly, we investigate the effect of the top cell bandgap on the tandem performance, showing that the best performance is attained at a 1.8 eV bandgap ($x = 0.78$). Then, the performance of $Ba(C_{0.78}Si_{0.22})_2/BaSi_2$ TSC is optimized through various steps including the effect of doping and the thickness of the absorber layers. Further, the current matching point is monitored whilst altering the thickness of the top cell. Finally, the impact of changing the absorber defect density of both cells and the work function of both contacts on the tandem performance is also discussed to highlight the possible routes for boosting the tandem efficiency.

## 2 Simulation methodology and device structure

### 2.1 Silvaco Atlas simulation methodology

The simulation study is performed by using the Silvaco Atlas simulation package which is a physics based 2- and 3-dimensional device simulator. The operating basis of this simulator is based on solving transport equations and Poisson's equation through a defined grid, allowing for depicting the physical processes related to device operation and giving reliable estimates about the device operation (Atlas User's Manual 2022). The physical models embedded in the simulation must be appropriately chosen to optimize the TSC. In this study, the principal physical models utilized for the design of a given solar cell structure are included. SRH recombination, the primary recombination mechanism in $BaSi_2$ (Hara et al. 2012), and the Fermi–Dirac statistics have been considered. Carriers' mobility and lifetime values within cell layers have been taken according to available experimental values (Takabe et al. 2014; Deng et al. 2018). In addition, Auger recombination (AUGER), optical recombination (OPTR), and concentration-dependent low-field mobility (CONMOB) models are enabled. Regarding the TSC, a lumped resistance was specified for the tunnel junction such that the current flows through the cell without considerable limitation (Elbar et al. 2015).

Firstly, our simulation was calibrated against an experimental $BaSi_2$/Si heterojunction cell with a structure of indium-doped tin oxide (ITO)/p-$BaSi_2$/n-Si/Aluminum (Al) metal back contact (Yachi et al. 2017). Figure 1a, b depict the device design and energy band diagram of the $BaSi_2$/Si heterojunction cell. The essential parameters of cell layers derived from previously published studies are summarized in Table 1 (Deng et al. 2018, 2020; Yachi et al. 2017). The work function of the ITO (transparent conducting front contact) is taken as 4.4 eV while that of the back Al metal is set to 4.28 eV. The absorption coefficients of the cell layers are derived from practical data (Toh et al. 2011; Vismara et al. 2016;

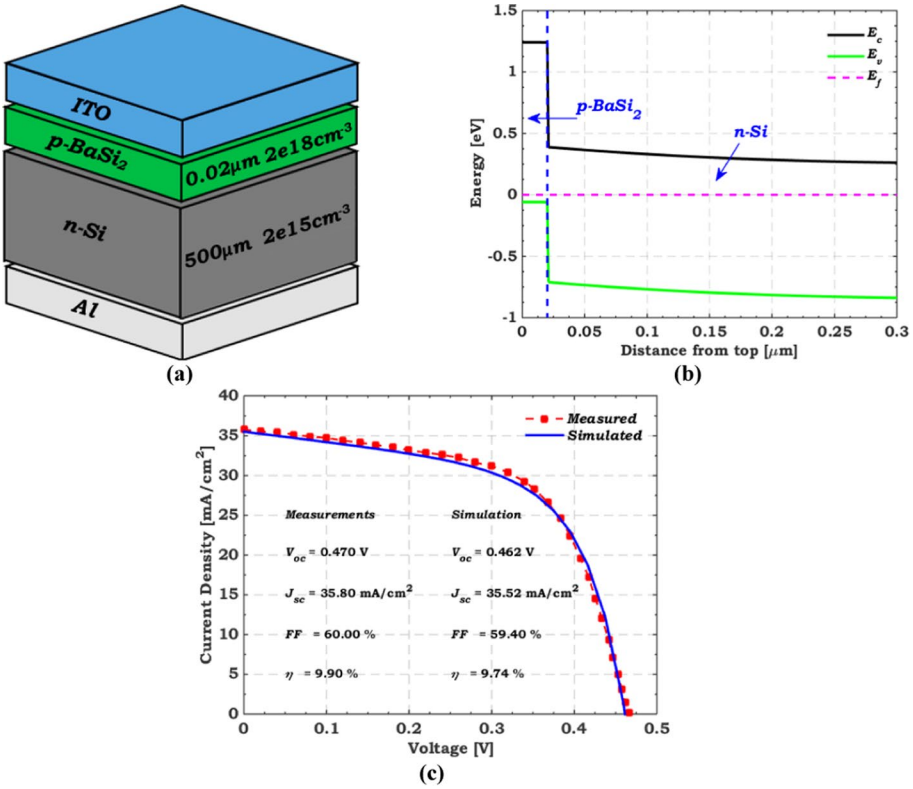


**Fig. 1** **a** structure indicating the design parameters and **b** Energy band diagram after contact at the dark condition of the p-$BaSi_2$/n-Si heterojunction solar cell. **c** Comparison of the simulated *J*–*V* characteristics with the measured data (Yachi et al. 2017) under AM 1.5 illumination condition

**Table 1** Basic parameters of the $BaSi_2$/Si heterojunction cell layers (Deng et al. 2018, 2020; Yachi et al. 2017)

| Material | p-$BaSi_2$ | n-Si |
|---|---|---|
| Thickness (μm) | 0.020 | 500 |
| Energy gap (eV) | 1.3 | 1.1 |
| Electron affinity (eV) | 3.2 | 4.05 |
| Relative permittivity | 14 | 11.7 |
| Electron mobility ($cm^2$/Vs) | 500 | 1000 |
| Hole mobility ($cm^2$/Vs) | 30 | 500 |
| CB effective density of states ($cm^{-3}$) | $2.6\times10^{19}$ | $2.8\times10^{19}$ |
| VB effective density of states ($cm^{-3}$) | $2.0\times10^{19}$ | $1.0\times10^{19}$ |
| Donor concentration $N_D$ ($cm^{-3}$) | – | $2.0\times10^{15}$ |
| Acceptor concentration $N_A$ ($cm^{-3}$) | $2.0\times10^{18}$ | – |

Green 2022). After applying the listed parameters, the illuminated current density–voltage (*J*–*V*) curves for both experimental and simulated cells are presented in Fig. 1c. The simulated cell achieves the following PV parameters: $J_{sc}=35.52$ mA/$cm^2$, $V_{oc}=0.462$ V, $FF=59.40\%$, and $\eta=9.74\%$. These parameters are quite close to the reported parameters,

as shown in the inset of Fig. 1c. As a result, an acceptable match between both cells is observed, implying that the simulation model employed in Silvaco Atlas software is validated.

### 2.2 Structures of two sub-cells

A homojunction solar cell with the $n^+$-p-$p^+$ architecture is introduced based on the practical structure of a $BaSi_2$ cell (Kodama et al. 2018). Figure 2 depicts the device design and energy band diagrams of the two sub-cells, containing an $n^+pp^+$-$BaSi_2$ bottom cell and an $n^+pp^+$-$Ba(C_xSi_{1-x})_2$ top cell. To create a homojunction solar cell, heavily doped $n^+$-and $p^+$-layers were positioned on opposite sides of a lightly doped p-absorber layer to extract photoexcited electron–hole pairs. The thickness of these layers was maintained at 20 nm, which was found experimentally to be the minimum thickness required to cover the entire surface adequately (Yachi et al. 2017). Table 2 summarizes the primary required parameters of the sub-cells layers used to design the tandem solar cell (Tianguo 2019; Yachi et al. 2017; Deng et al. 2020). To model the optical properties, the refractive index *n'* and extinction coefficient $\kappa$ as functions of a wavelength of barium di-silicide were extracted

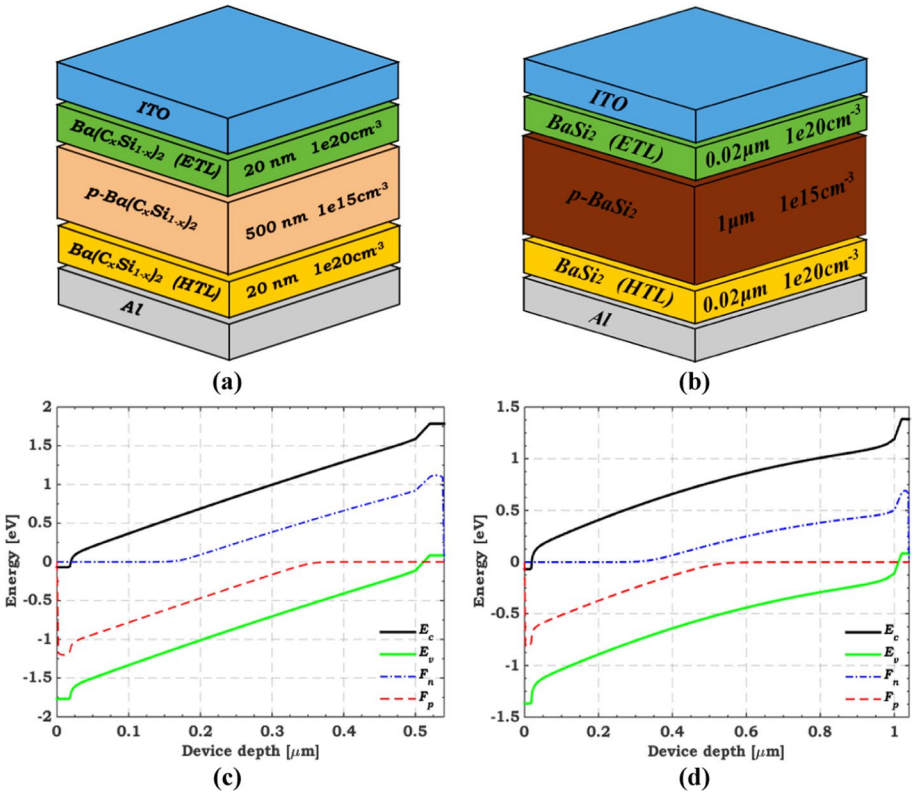


**Fig. 2** The main configuration of **a** $Ba(C_xSi_{1-x})_2$ top cell, and **b** $BaSi_2$ bottom cell, indicating the design parameters. The energy band diagram at the short-circuit condition of **c** $Ba(C_xSi_{1-x})_2$ top cell, and **d** $BaSi_2$ bottom cell, where $F_n$ and $F_p$ represent the electron and hole quasi-Fermi levels, respectively

**Table 2** Primary parameters of the sub-cells' layers used for the design of $Ba(C_xSi_{1-x})_2/BaSi_2$ tandem solar cell (Tianguo 2019; Yachi et al. 2017; Deng et al. 2020)

| Parameters | Top cell ($Ba(C_xSi_{1-x})_2$) | | | Bottom cell ($BaSi_2$) | | |
|---|---|---|---|---|---|---|
| | $n^+$ | p | $p^+$ | $n^+$ | p | $p^+$ |
| Thickness (μm) | 0.02 | 0.5 | 0.02 | 0.02 | 1 | 0.02 |
| Energy gap (eV) | Variable | Variable | Variable | 1.3 | 1.3 | 1.3 |
| Electron affinity (eV) | 3.2 | 3.2 | 3.2 | 3.2 | 3.2 | 3.2 |
| Relative permittivity | 14 | 14 | 14 | 14 | 14 | 14 |
| Electron mobility ($cm^2/Vs$) | 500 | 850 | 600 | 500 | 850 | 600 |
| Hole mobility ($cm^2/Vs$) | 20 | 100 | 30 | 20 | 100 | 30 |
| Electron lifetime (μs) | 3 | 8 | 2 | 3 | 8 | 2 |
| Hole lifetime (μs) | 3 | 8 | 2 | 3 | 8 | 2 |
| CB effective density of states ($cm^{-3}$) | $2.6\times10^{19}$ | $2.6\times10^{19}$ | $2.6\times10^{19}$ | $2.6\times10^{19}$ | $2.6\times10^{19}$ | $2.6\times10^{19}$ |
| VB effective density of states ($cm^{-3}$) | $2.0\times10^{19}$ | $2.0\times10^{19}$ | $2.0\times10^{19}$ | $2.0\times10^{19}$ | $2.0\times10^{19}$ | $2.0\times10^{19}$ |
| Donor doping concentration $N_D$ ($cm^{-3}$) | $1.0\times10^{20}$ | – | – | $1.0\times10^{20}$ | – | – |
| Acceptor doping concentration $N_A$ ($cm^{-3}$) | – | $1.0\times10^{15}$ | $1.0\times10^{20}$ | – | $1.0\times10^{15}$ | $1.0\times10^{20}$ |

from experimental data (Toh et al. 2011; Vismara et al. 2016; Tianguo 2019), where $\kappa$ was calculated from the relationship $\alpha = 4\pi\kappa/\lambda$.

### 2.3 Proposed tandem cell

In this subsection, the suggested structure of the tandem cell design ($Ba(C_xSi_{1-x})_2/BaSi_2$) is displayed in Fig. 3. In this tandem cell, the two cells are coupled through a tunnel junction that performs as a recombination film (Mailoa et al. 2015). The practical design of the tunnel junction is a critical task in order to maintain proper functionality leading to the enhancement of the tandem performance (Shen et al. 2018). The junction has to be transparent, and it should not absorb any part of the input radiation spectrum reaching the bottom cell. Such requirements have been met by fulfilling two design conditions: (1) the tunnel junction has to be heavily doped, and (2) both sides of the junction should be very thin in the nanometer range (Wang et al. 2012). Furthermore, the tandem cell current is controlled by the smaller current transporting through either the top or the bottom sub-cell. Once stacking the two sub-cells, the current matching condition should be maintained to minimize the current loss.

## 3 Results and discussion

First, we investigate the effect of the top cell bandgap on the tandem performance to design the tandem device for possible maximum efficiency. Then, the tandem performance of the cell is optimized through various steps including the effect of doping and the thickness of the absorber layers, changing the absorber defect density of both cells, and the work function of both contacts to obtain the maximum available $\eta$.

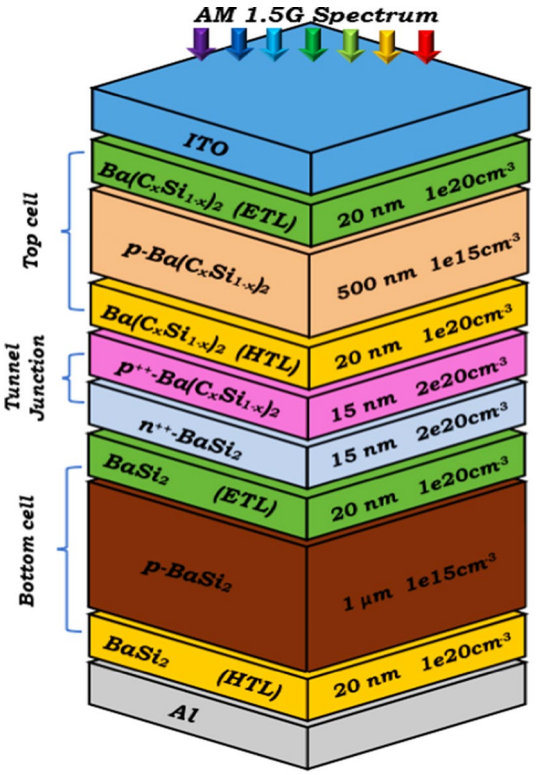


**Fig. 3** Schematic representation of a $Ba(C_xSi_{1-x})_2/BaSi_2$ tandem cell comprising of an $n^+pp^+$-$Ba(C_xSi_{1-x})_2$ top sub-cell and an $n^+pp^+$-$BaSi_2$ bottom sub-cell (ETL and HTL represent electron transport and hole transport layer, respectively)

### 3.1 Tandem cell with different bandgap top cell

In this subsection, we investigate the effect of the top cell bandgap on the tandem performance where the compound $Ba(C_xSi_{1-x})_2$ as a top absorber is adopted. The variation of the top cell absorber bandgap depends on the composition (x) (Imai and Watanabe 2010). Here, the $Ba(C_xSi_{1-x})_2$top cell bandgap is varied from 1.6 to 1.9 eV, which corresponds to x from 0.73 to 0.80. So, the $Ba(C_xSi_{1-x})_2/BaSi_2$ tandem cells are simulated using Atlas device simulator under 1-sun of AM1.5G spectrum to evaluate its performance parameters. The absorber thickness of the top cell was set to 500 nm, while the bottom $BaSi_2$ was fixed at 1 µm. Figure 4a, b depict a comparison between the illuminated *J–V* and *EQE* curves concerning the $Ba(C_xSi_{1-x})_2/BaSi_2$ tandem cells. The corresponding performance metrics are listed in Table 3. The results show that the best performance is obtained with a $Ba(C_{0.78}Si_{0.22})_2$ cell with a 1.8 eV bandgap. These complementary bandgap values agree with those reported in Eperon et al. (2017) to achieve the maximum theoretical $\eta$. In the coming simulations, this value will be used for further optimization of the TSC under investigation.

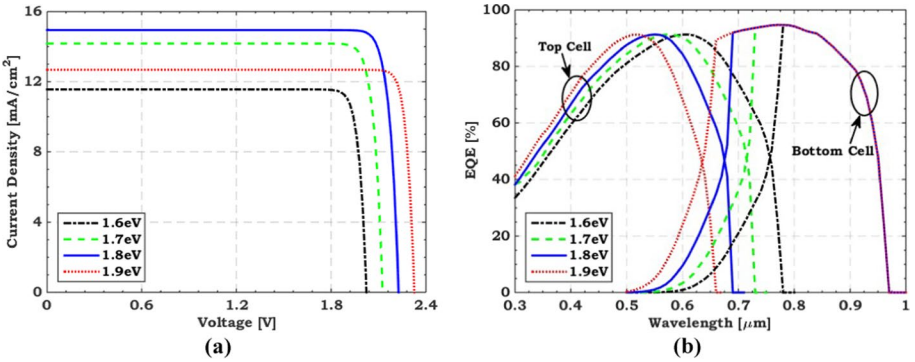


**Fig. 4** **a** Illuminated *J–V*, and **b** *EQE* curves of a $Ba(C_xSi_{1-x})_2/BaSi_2$ tandem cell

**Table 3** A comparison between the performance metrics for $Ba(C_xSi_{1-x})_2/BaSi_2$ tandem cells

| $Ba(C_xSi_{1-x})_2$ Top cell | | $J_{sc}$ (mA/cm$^2$) | $V_{oc}$ (V) | *FF* (%) | $\eta$ (%) |
|---|---|---|---|---|---|
| x | $E_g$ (eV) | | | | |
| 0.73 | 1.6 | 11.56 | 2.02 | 90.71 | 21.21 |
| 0.76 | 1.7 | 14.18 | 2.13 | 90.08 | 27.14 |
| 0.78 | 1.8 | 14.94 | 2.23 | 90.20 | 30 |
| 0.80 | 1.9 | 12.68 | 2.33 | 92 | 27.13 |

## 3.2 Tandem cell optimization

This subsection presents the following optimization steps for a 2T monolithic $Ba(C_xSi_{1-x})_2/BaSi_2$ TSC. First, the impact of the absorber layers doping on the tandem performance is studied. Then, we investigate the influence of top and bottom absorber thicknesses on TSC working metrics. Furthermore, we inspect the current matching point to get the maximum available $\eta$. The effect of top and bottom absorber defect densities on TSC working metrics is then investigated. Finally, we study the impact of front and rear contact work functions on the TSC performance.

### 3.2.1 Doping of absorber layers

The absorber layer doping is crucial in regulating bulk recombination. Its role in controlling the fill factor is also significant as increasing the doping level results in decreasing the series resistance which, in turn, increases the fill factor. However, increasing the doping level beyond a certain value may trigger some other undesirable effects like band gap narrowing and mobility degradation that causes an overall decline in performance. Herein, a parametric analysis study is done by changing the absorber layers doping from $1\times10^{15}$ to $1\times10^{19}$ cm$^{-3}$ to investigate its impact on the tandem performance. Figure 5a, b demonstrate that the $\eta$ attains its maximum value when the doping density is $1\times10^{17}$ cm$^{-3}$ for both cells. To inspect the influence of changing the absorber layers doping on the tandem

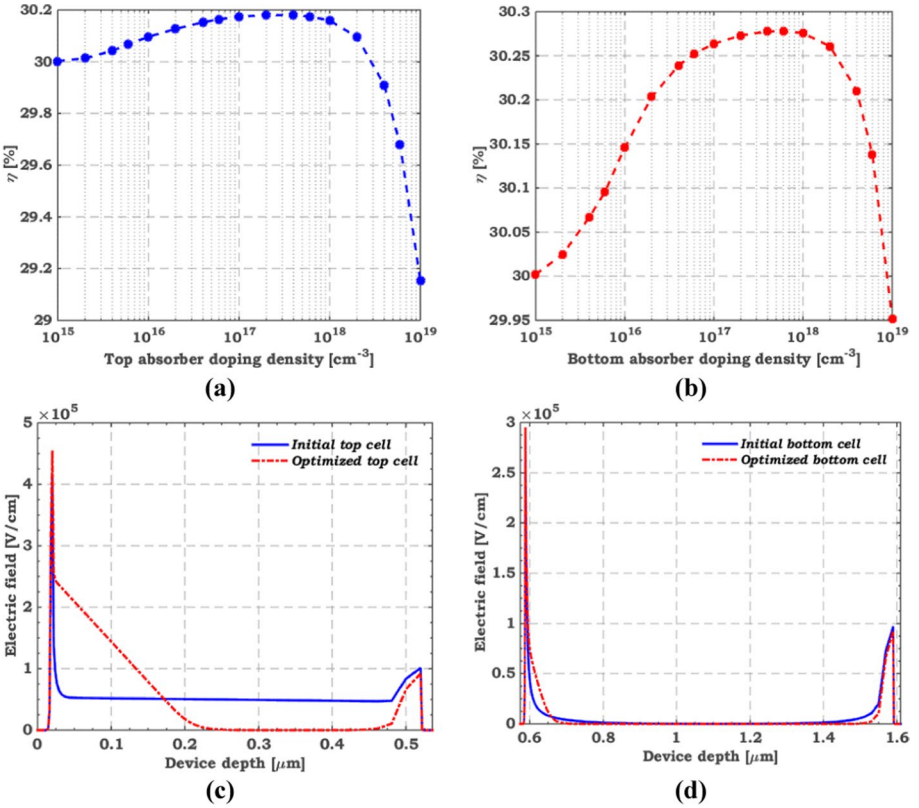


**Fig. 5** Impact of the doping density of the absorber on $\eta$ of **a** $Ba(C_{0.78}Si_{0.22})_2$ top cell, and **b** $BaSi_2$ bottom cell. The electric field before and after optimization of **c** $Ba(C_{0.78}Si_{0.22})_2$ top cell, and **d** $BaSi_2$ bottom cell for the short-circuit condition under illumination

performance, the electric field under light illumination before and after optimization is depicted in Fig. 5c, d. The electric field in a depletion region is responsible for separating photogenerated carriers and, in addition, depends on the carrier's doping on both junction sides. As shown in Fig. 5c, d, increasing absorber doping increases the depletion region width and thus increases its electric field for both sub-cells and, consequently, improves their conversion efficiency.

### 3.2.2 The thickness of the absorber layers

Figure 6 represents a contour graph of TSC efficiency dependence on the thickness of both the top and bottom absorber layers. To investigate device performance, the thickness of the top absorber was increased from 0.5 up to 1.6 μm and that of the bottom absorber was increased from 1 to 4 μm while the other parameters remained constant. As obvious from Fig. 6, there is an inconsiderable effect on $\eta$ as the thickness of the rear absorber grows from 2 to 4 μm and that of the front absorber raises from 0.8 to 1.6 μm. As the bottom absorber thickness falls below 0.8 μm, the efficiency gradually decreases from 32.4 to 30.4%. Furthermore, there is no change in $\eta$ as the bottom absorber thickness changes from

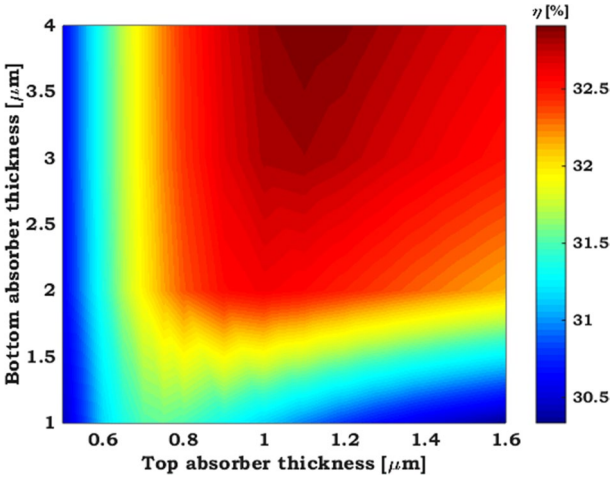


**Fig. 6** Contour graph of TSC efficiency dependency on the thickness of the top and bottom absorber layers

2 to 4 µm, while the thickness of the bottom absorber layer remains constant below 0.8 µm. The best performance can be determined when the thicknesses of the top and bottom cells are chosen to be 1.1 and 3 µm, respectively.

### 3.2.3 Current matching point

In this subsection, the absorber thickness ($d$) of the top cell has been altered from 0.85 to 1.25 µm, while the bottom $BaSi_2$ was fixed at 3 µm. Figure 7a shows the $J_{sc}$ of the top and bottom sub-cells versus the thickness of the $Ba(C_{0.78}Si_{0.22})_2$ absorber layer in the top cell, in which significant dependency on $d$ is shown. As $d$ becomes thicker, the $J_{sc}$ of the top cell rises, and the $J_{sc}$ of the bottom cell, in turn, reduces. The reason is that the thicker the top cell is, the more photons are absorbed implying lesser transferred light to the bottom cell. A current matching point occurs at $J_{sc} = 16.47$ mA/cm$^2$ and is satisfied at $d = 1.05$ µm for the absorbing film of the top cell. As displayed in Fig. 7b, $\eta$ of the tandem cell reaches a maximum value at the current matching point. In this condition, the performance of the $Ba(C_{0.78}Si_{0.22})_2/BaSi_2$ tandem cell has been simulated. The $J$–$V$ characteristics of tandem, top, and bottom cells are drawn in Fig. 7c. The maximum value of $J_{sc}$ of tandem, top, and bottom cells is equal to 16.47 mA/cm$^2$ with $V_{oc} = 2.24$ V and $\eta = 32.83\%$ for the tandem cell. The value of $V_{oc} = 2.24$ V is equal to the sum of those of the top cell (1.37 V) and bottom cell (0.87 V), indicating the efficient operation of the recombination junction. Moreover, the *EQE* of both cells at the current matching condition is demonstrated in Fig. 7d. The *EQE* of the bottom $BaSi_2$ sub-cell surpasses 95% at a wavelength around 800 nm.

Figure 8a illustrates the structure of the $Ba(C_{0.78}Si_{0.22})_2/BaSi_2$ tandem cell produced by the Atlas simulator at the current matching point. As the bottom $BaSi_2$ cell is exceedingly thicker than the top sub-cell, the extended view of the red dashed area in Fig. 8a is displayed in Fig. 8b.

Figure 8c depicts the electrostatic potential established through the TSC. The built-in potential of the tunnel junction indicates a greater potential in this specific region. Meanwhile, the electrostatic potential decreases as one proceeds in two directions away from the tunnel junction. Additionally, Fig. 8d displays the photogeneration rate inside the different layers. The graph reveals that the top $Ba(C_{0.78}Si_{0.22})_2$ cell has a greater photogeneration rate

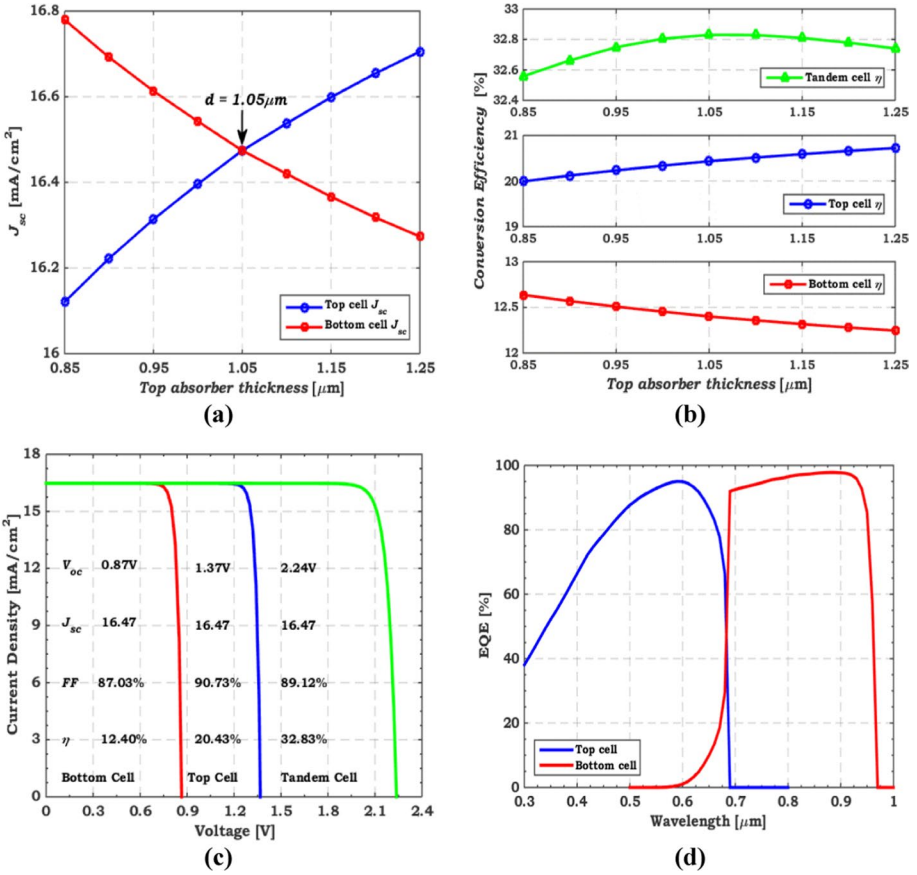


**Fig. 7** Variation of cell parameters versus $d$ of top cell absorber layer from 0.85 to 1.25 μm **a** $J_{sc}$ of top and bottom sub-cells and **b** $\eta$ of the bottom, top and tandem cells. Device characteristics at the current matching point **c** *J–V* of the bottom, top, and tandem cells and **d** *EQE* spectra of bottom and top cells

than the bottom $BaSi_2$ cell. Photogenerated carriers recombine in the tunnel junction area. A low photogeneration rate has been observed as a result of this recombination.

### 3.2.4 The defect density of the absorber layers

Figure 9 represents contour graphs of TSC performance metrics dependence on the defect concentration of both the top and bottom absorber layers. The defect density ranges from $10^{12}$ to $10^{18}$ cm$^{-3}$ while preserving the other parameters unchanged to explore the device performance. As clear from Fig. 9a, the $J_{sc}$ significantly decreases as the defect density of the top and bottom absorber layers increases. For example, $J_{sc}$ drops from 16 to 12 mA/cm$^2$ as the defect density of the bottom absorber rises from $10^{15}$ to $10^{18}$ cm$^{-3}$, and that of the top layer grows from $10^{16}$ to $10^{18}$ cm$^{-3}$. Besides, there is no change in $J_{sc}$ as the defect density of the top absorber layer is below $10^{16}$ cm$^{-3}$ or that of the bottom absorber layer is below $10^{15}$ cm$^{-3}$.

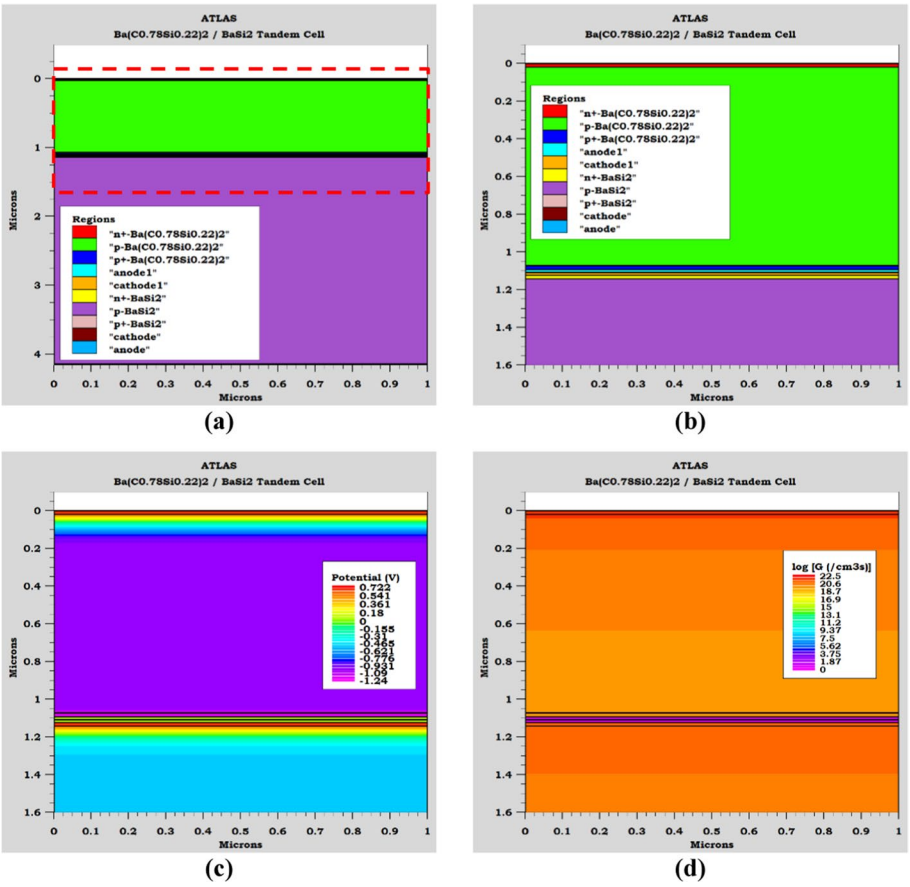


**Fig. 8** **a** TSC architecture created by Atlas. **b** Expanded picture of the red dashed area in **a**. **c** Electrostatic potential distribution and **d** photogeneration rate (G) inside the tandem cell with a magnified view

It has been reported in the literature that $V_{oc}$ is extremely affected by the defect concentration of the absorber layer (Soucase et al. 2016). In this context, it can be shown in Fig. 9b that $V_{oc}$ decreases from 2.10 to 1.55 V when the defect density of the absorber layers raises from $10^{15}$ to $10^{18}$ $cm^{-3}$. For absorber layers defect density lower than $10^{15}$ $cm^{-3}$, there is no appreciable effect on $V_{oc}$. Figure 9c shows that the *FF* gradually declines from 86 to 73% when the defect density of the absorber layers raises from $10^{15}$ to $10^{18}$ $cm^{-3}$. Again, for small values of defect density of absorber layers (below $10^{15}$ $cm^{-3}$), there is no significant effect on *FF*. Theoretically, *FF* is solely a function of $V_{oc}$, however, *FF* is not only related to $V_{oc}$ but in addition, it is strongly correlated to the recombination processes inside the depletion region.

Finally, as clarified in Fig. 9d, we noticed an expected changing profile in $\eta$ due to its dependency on $J_{sc}$, $V_{oc}$, and *FF*. There is an insignificant effect on $\eta$ as the defect density of the absorber layers is below $10^{15}$ $cm^{-3}$. $\eta$ sharply decreases from 30 to 13% as the defect density of the absorber layers grows from $10^{15}$ to $10^{18}$ $cm^{-3}$.

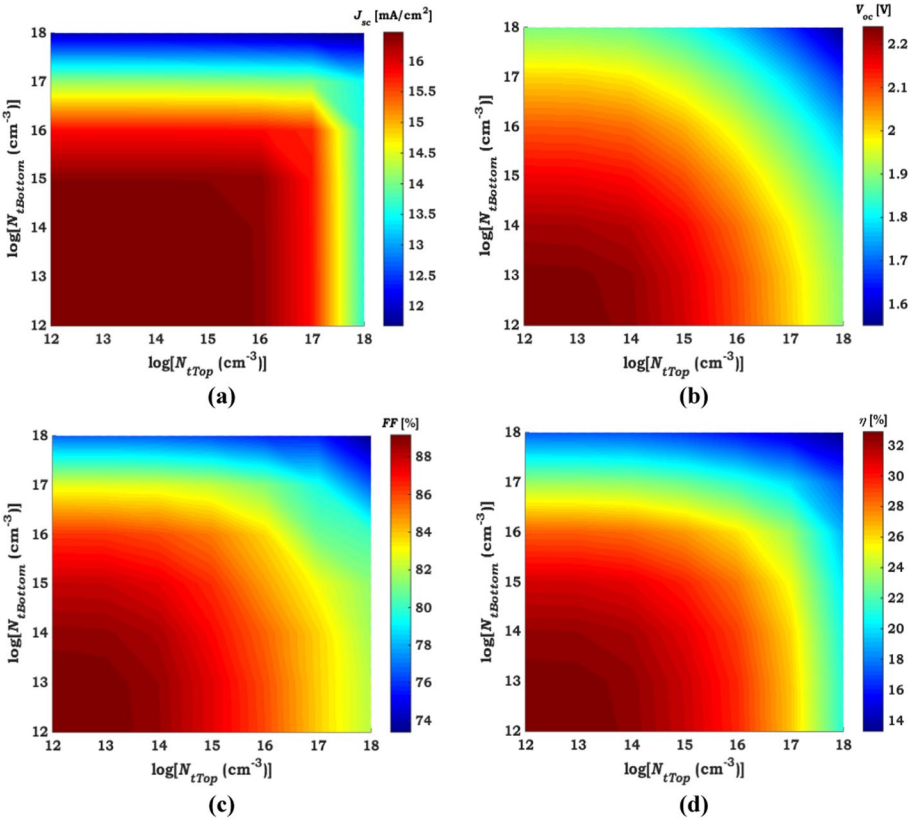


**Fig. 9** Contour graphs of TSC performance figure of merit dependency on the defect density of top and bottom absorber layers

### 3.2.5 Work functions of the front and rear contacts

Work functions of the front and rear contacts are crucial factors that affect the device's performance as they modulate the metal/semiconductor contact barrier height and therefore the transportation of charge carriers (Anwar et al. 2017). The front Schottky barrier at the metal/n$^+$-Ba($C_{0.78}Si_{0.22}$)$_2$ interface is computed using the equation (Liao et al. 2020):

$$\phi_{\mathrm{b,front}} = \varphi_{\mathrm{m,front}} - \chi \tag{1}$$

where $\varphi_{\mathrm{m,\,front}}$ is the front contact work function, and $\chi$ is the electronic affinity of Ba($C_{0.78}Si_{0.22}$)$_2$. while the rear Schottky barrier at the metal/p$^+$-$BaSi_2$ interface is calculated using the equation (Liao et al. 2020):

$$\phi_{\mathrm{b,rear}} = \chi + E_g - \varphi_{\mathrm{m,rear}} \tag{2}$$

where $\chi$ and $E_g$ are the electronic affinity and the bandgap energy of $BaSi_2$, respectively, and $\varphi_{\mathrm{m,\,rear}}$ is the rear contact work function. The front contact work function is changed from 3 to 4.8 eV, while that of the rear contact materials is summarized in Table 4.

**Table 4** Inorganic rear contact materials showing their work function values and indicating the corresponding references from the literature (Anwar et al. 2017; Sawicka-Chudy et al. 2019; Salem et al. 2022; Derry et al. 2015; Singh et al. 2019)

| Material | Work function (eV) |
|---|---|
| Al (aluminum) | 4.28 |
| Mo (Molybdenum) | 4.6 |
| Ag (silver) | 4.74 |
| Fe (iron) | 4.81 |
| Nb (niobium) | 4.9 |
| Cu (copper) | 5 |
| Au (gold) | 5.1 |
| Pd (palladium) | 5.3 |
| C (carbon) | 5.4 |
| Ni (nickel) | 5.5 |
| Pt (platinum) | 5.7 |

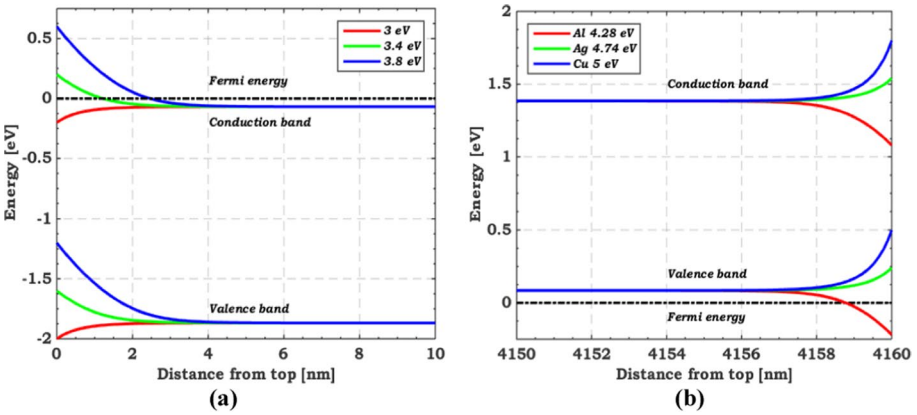


**Fig. 10** Energy band diagram at short-circuit and dark conditions of **a** the top 10 nm for different values of front contact work function, and **b** the bottom 10 nm for distinct values of rear contact work function

Figure 10a, b illustrate the energy band diagrams for various work function values of front and rear contacts at the short circuit and dark conditions. As apparent in Fig. 10a, increasing $\varphi_{m,front}$ results in increasing the front barrier height $\phi_{b,front}$, which leads to sufficient bending up of $E_c$ close to metal/$n^+$-$Ba(C_{0.78}Si_{0.22})_2$ interface irrespective of $n^+$-$Ba(C_{0.78}Si_{0.22})_2$ thickness. This bending impedes the transfer of photo-excited electrons to the front electrode. On the other hand, decreasing $\varphi_{m,front}$ leads to a decrease of $\phi_{b,front}$, and thus, improves the device performance. Similarly, in Fig. 10b, the rear barrier height $\phi_{b,\,rear}$ produces sufficient bending down of $E_v$ adjoining to the $p^+$-$BaSi_2$/metal interface and so the series resistance increases at the contact interface which results in impeding the transport of photoexcited holes to the back electrode. In addition, $\phi_{b,\,rear}$ decreases with increasing $\varphi_{m,\,rear}$ and improves the device performance.

Figure 11 exhibits contour graphs of the photovoltaic parameters of $Ba(C_{0.78}Si_{0.22})_2$/$BaSi_2$ tandem solar cells under different values of the work function for both contacts. As apparent in Fig. 11, there is no effect on the performance parameters as $\varphi_{m,\,rear}$ is larger

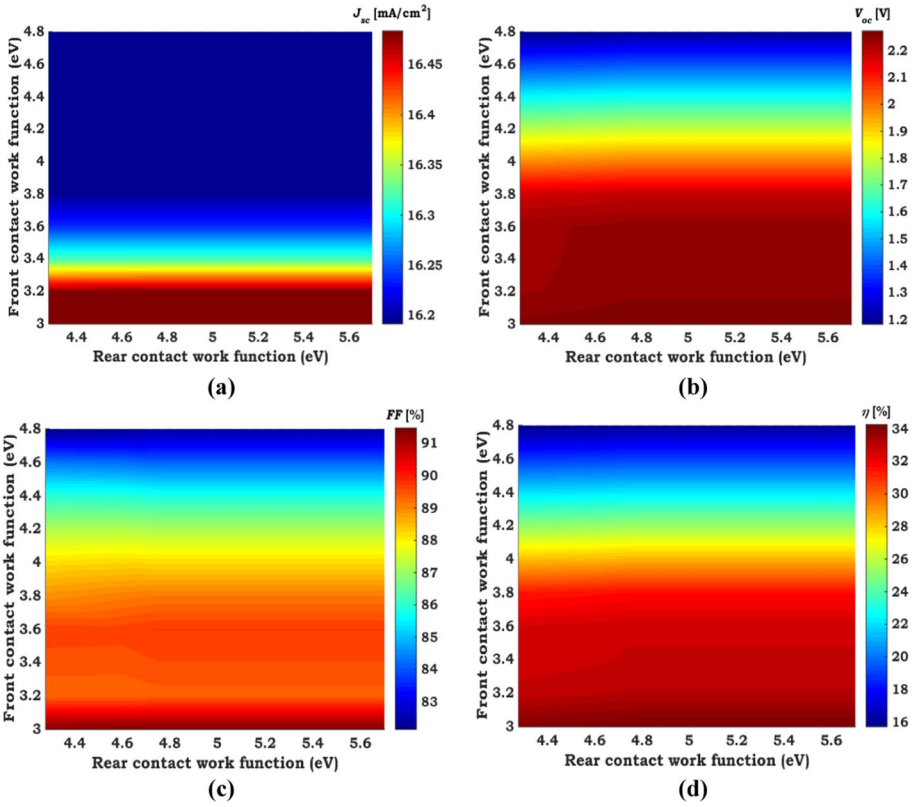


**Fig. 11** Contour graphs of tandem cell performance parameters dependence on front and rear contact work function

than 4.5 eV while $\varphi_{m,front}$ remains constant. On the other hand, with increasing $\varphi_{m,front}$ from 3.8 to 4.8 eV, $J_{sc}$ and $FF$ values gradually decrease while $V_{oc}$ drastically drops from 2.18 to 1.18 V. Finally, as clarified in Fig. 11d, an expected trend in $\eta$ is observed due to its dependency on $J_{sc}$, $V_{oc}$, and $FF$. There is an insignificant effect on $\eta$ when $\varphi_{m,front}$ is below 3.8 eV, and $\varphi_{m,\,rear}$ remains constant, while it sharply decreases from 31 to 15% as $\varphi_{m,front}$

**Table 5** A state-of-art comparison between performance parameters of $Ba(C_{0.78}Si_{0.22})_2/BaSi_2$ tandem cell and some multi-junction solar cells stated in the literature

| Material | Method | $J_{sc}$ (mA/cm$^2$) | $V_{oc}$ (V) | $FF$ (%) | $\eta$ (%) | References |
|---|---|---|---|---|---|---|
| Lead-based perovskite/Si | Exp | 15.80 | 1.692 | 79.90 | 21.4 | Cheng and Ding (2021) |
| $GaAs_{0.75}P_{0.25}$/Si | Exp | 17.34 | 1.732 | 77.70 | 23.4 | Green et al. (2022) |
| Lead-based perovskite/Si | Exp | 18.14 | 1.753 | 78.50 | 25.0 | Cheng and Ding (2021) |
| Lead-free perovskite/Si | Sim | 16.01 | 1.76 | 86.7 | 24.4 | Amri et al. (2021) |
| Lead-based perovskite/CIGS | Sim | 20.49 | 1.81 | 81.8 | 30.5 | Mousa et al. (2020) |
| $Ba(C_{0.75}Si_{0.25})_2$/Si | Sim | 17.6 | 1.94 | 88.4 | 30.3 | Tianguo (2019) |
| $Ba(C_{0.78}Si_{0.22})_2/BaSi_2$ | Sim | 16.48 | 2.27 | 91.45 | 34.25 | This work |

is increased above 3.8 eV. The optimum efficiency has been attained with a terbium front contact ($\varphi_{terbium} = 3$ eV) and a silver rear contact, resulting in the following PV parameters: $J_{sc} = 16.48$ mA/cm$^2$, $V_{oc} = 2.27$ V, $FF = 91.45\%$, and $\eta = 34.25\%$.

Finally, we provide a comparison between our optimized TSC and other tandem candidates, as shown in Table 5. Some of the reported tandem cells are based on experimental investigations, while others are computed numerically, as illustrated in the table. Most tandem cells with lead-based perovskite top cells give higher efficiencies; however, the toxicity of such tandems is a serious issue that limits their use and commercialization. Moreover, our simulated tandem solar cell shows promising properties with a high $\eta$ and $V_{oc}$.

## 4 Conclusion

In this work, all-$BaSi_2$ 2T monolithic tandem solar cell is presented. In the proposed design, the bottom cell comprises $BaSi_2$ material with a 1.3 eV bandgap, while for the top cell, $Ba(C_{0.78}Si_{0.22})_2$ with a 1.8 eV bandgap is employed. After optimizing the doping and the thickness of both absorber layers, and at the designed matching point, the current density and $\eta$ of the TSC are enhanced up to 16.47 mA/cm$^2$ and 32.83%, respectively. Additionally, we have inspected the consequence of the absorbers defect density in the range ($10^{12}$–$10^{18}$ cm$^{-3}$) and the impact of the work functions of the contacts on the performance parameters of the TSC. It was found that contacts having a work function $\geq 4.5$ eV for rear contact and $\leq 3.8$ eV for front contact were adequate for better performance. These results can offer possible routes leading in the direction of the advancement of low-cost, environmentally friendly, and efficient TSCs.

**Author contributions** MO, AS and TMA wrote the main manuscript text. MO, ISA and MSS performed the simulation and prepared the figures. All authors shared in conceptualization, methodology, and validation. All authors reviewed the manuscript.

**Funding** Open access funding provided by The Science, Technology & Innovation Funding Authority (STDF) in cooperation with The Egyptian Knowledge Bank (EKB). Not Applicable.

**Availability of data and materials** Data will be made available on reasonable request.

## Declarations

**Conflict of interest** The authors declare that they have no known competing financial interests.

**Ethical approval** Not Applicable.

## References


Amri, K., Belghouthi, R., Aillerie, M., Gharbi, R.: Device optimization of a lead-free perovskite/silicon tandem solar cell with 24.4% power conversion efficiency. Energies **14**(12), 3383 (2021). https://doi.org/10.3390/en14123383

Anwar, F., Afrin, S., Satter, S.S., Mahbub, R., Ullah, S.M.: Simulation and performance study of nanowire CdS/CdTe solar cell. Int. J. Renew. Energy Res. **7**(2), 885–893 (2017)

Atlas User's Manual, Silvaco Inc., Santa Clara, USA. https://silvaco.com/products/tcad/device_simulation/atlas/atlas.html. Accessed 1 June 2022

Baba, M., Toh, K., Toko, K., Saito, N., Yoshizawa, N., Jiptner, K., Sekiguchi, T., Hara, K.O., Usami, N., Suemasu, T.: Investigation of grain boundaries in $BaSi_2$ epitaxial films on Si(111) substrates using transmission electron microscopy and electron-beam-induced current technique. J. Cryst. Growth **348**(1), 75–79 (2012). https://doi.org/10.1016/j.jcrysgro.2012.03.044

Cheng, Y., Ding, L.: Perovskite/Si tandem solar cells: fundamentals, advances, challenges, and novel applications. SusMat **1**(3), 324–344 (2021). https://doi.org/10.1002/sus2.25

Deng, T., Suemasu, T., Shohonov, D.A., Samusevich, I.S., Filonov, A.B., Migas, D.B., Borisenko, V.E.: Transport properties of n- and p-type polycrystalline $BaSi_2$. Thin Solid Films **661**, 7–15 (2018). https://doi.org/10.1016/j.tsf.2018.07.006

Deng, T., Xu, Z., Yamashita, Y., Sato, T., Toko, K., Suemasu, T.: Modeling the effects of defect parameters on the performance of a p-$BaSi_2$/n-Si heterojunction solar cell. Sol. Energy Mater. Sol. Cells **205**, 110244 (2020). https://doi.org/10.1016/j.solmat.2019.110244

Derry, G.N., Kern, M.E., Worth, E.H.: Recommended values of clean metal surface work functions. J. Vac. Sci. Technol. A Vacuum Surfaces Film **33**(6), 060801 (2015). https://doi.org/10.1116/1.4934685

Elbar, M., Tobbeche, S., Merazga, A.: Effect of top-cell CGS thickness on the performance of CGS/CIGS tandem solar cell. Sol. Energy **122**, 104–112 (2015). https://doi.org/10.1016/j.solener.2015.08.029

Eperon, G.E., Hörantner, M.T., Snaith, H.J.: Metal halide perovskite tandem and multiple-junction photovoltaics. Nat. Rev. Chem. **1**(12), 0095 (2017). https://doi.org/10.1038/S41570-017-0095

Farooq, W., Alshahrani, T., Kazmi, S.A.A., Iqbal, J., Khan, H.A., Khan, M., Raja, A.A., Ur Rehman, A.: Materials Optimization for thin-film copper indium gallium selenide (CIGS) solar cell based on distributed braggs reflector. Optik **227**, 165987 (2021). https://doi.org/10.1016/j.ijleo.2020.165987

Gamal, N., Sedky, S.H., Shaker, A., Fedawy, M.: Design of lead-free perovskite solar cell using $Zn_{1-x}Mg_xO$ as ETL: SCAPS device simulation. Optik **242**, 167306 (2021). https://doi.org/10.1016/j.ijleo.2021.167306

Green, M.A.: Improved silicon optical parameters at 25°C, 295 K and 300 K including temperature coefficients. Prog. Photovoltaics Res. Appl. **30**(2), 164–179 (2022). https://doi.org/10.1002/pip.3474

Green, M.A., Dunlop, E.D., Hohl-Ebinger, J., Yoshita, M., Kopidakis, N., Bothe, K., Hinken, D., Rauer, M., Hao, X.: Solar cell efficiency tables (Version 60). Prog. Photovolt. Res. Appl. **30**(7), 687–701 (2022). https://doi.org/10.1002/pip.3595

Hara, K.O., Usami, N., Toh, K., Baba, M., Toko, K., Suemasu, T.: Investigation of the recombination mechanism of excess carriers in undoped $BaSi_2$ films on silicon. J. Appl. Phys. **112**(8), 083108 (2012). https://doi.org/10.1063/1.4759246

Hara, K.O., Usami, N., Nakamura, K., Takabe, R., Baba, M., Toko, K., Suemasu, T.: Determination of bulk minority-carrier lifetime in $BaSi_2$ earth-abundant absorber films by utilizing a drastic enhancement of carrier lifetime by post-growth annealing. Appl. Phys. Exp. **6**(11), 112302 (2013). https://doi.org/10.7567/APEX.6.112302

Huang, X.: Design and development of high performance III-nitrides photovoltaics. PhD diss., Arizona State University. (2020)

Imai, Y., Watanabe, A.: Assessment of the possibility of band gap widening of $BaSi_2$ by incorporation of carbon. Intermetallics **18**(8), 1432–1436 (2010). https://doi.org/10.1016/j.intermet.2010.03.019

Khan, M.A., Saito, T., Nakamura, K., Baba, M., Du, W., Toh, K., Toko, K., Suemasu, T.: Electrical characterization and conduction mechanism of impurity-doped $BaSi_2$ films grown on Si(111) by molecular beam epitaxy. Thin Solid Films **522**, 95–99 (2012). https://doi.org/10.1016/j.tsf.2012.09.005

Kodama, K., Takabe, R., Deng, T., Toko, K., Suemasu, T.: Spectroscopic evidence of photogenerated carrier separation by built-in electric field in Sb-doped n-$BaSi_2$/B-doped p-$BaSi_2$ homojunction diodes. Jpn. J. Appl. Phys. **57**(5), 050310 (2018). https://doi.org/10.7567/JJAP.57.050310

Kumar, M., Umezawa, N., Imai, M.: (Sr, Ba)$(Si, Ge)_2$ for thin-film solar-cell applications: first-principles study. J. Appl. Phys. **115**(20), 203718 (2014). https://doi.org/10.1063/1.4880662

Liao, H., Deng, Q., Shen, Y., Wang, G., Wang, S., Mao, Y.: Theoretical analysis of doping concentration, layer thickness and barrier height effects on $BaSi_2$ based homojunction solar cells toward high efficiency. Sol. Energy. **201**, 857–865 (2020). https://doi.org/10.1016/j.solener.2020.03.056

Mailoa, J.P., Bailie, C.D., Johlin, E.C., Hoke, E.T., Akey, A.J., Nguyen, W.H., McGehee, M.D., Buonassisi, T.: A 2-terminal perovskite/silicon multijunction solar cell enabled by a silicon tunnel junction. Appl. Phys. Lett. **106**(12), 121105 (2015). https://doi.org/10.1063/1.4914179

Morita, K., Kobayashi, M., Suemasu, T.: Effects of Sr addition on crystallinity and optical absorption edges in ternary semiconducting silicide $Ba_{1-x}Sr_xSi_2$. Thin Solid Films **515**(22), 8216–8218 (2007). https://doi.org/10.1016/j.tsf.2007.02.047

Mousa, M., Salah, M.M., Amer, F.Z., Saeed, A., Mubarak, R.I.: High efficiency tandem perovskite/CIGS solar cell. In: 2020 2nd Int. Conf. Smart Power Internet Energy Syst. SPIES 2020. 224–227 (2020). https://doi.org/10.1109/SPIES48661.2020.9242927

Okil, M., Salem, M.S., Abdolkader, T.M., Shaker, A.: From crystalline to low-cost silicon-based solar cells: a review. Silicon **14**, 1895-1911 (2022). https://doi.org/10.1007/s12633-021-01032-4

Pathi, P., Peer, A., Biswas, R.: Nano-photonic structures for light trapping in ultra-thin crystalline silicon solar cells. Nanomaterials **7**(1), 17 (2017). https://doi.org/10.3390/nano7010017

Salem, M.S., Shaker, A., Othman, M.S., Al-Bagawia, A.H., Fedawy, M., Aleid, G.M.: Numerical analysis and design of high performance HTL-free antimony sulfide solar cells by SCAPS-1D. Opt. Mater. **123**, 111880 (2022). https://doi.org/10.1016/j.optmat.2021.111880

Sawicka-Chudy, P., Starowicz, Z., Wisz, G., Yavorskyi, R., Zapukhlyak, Z., Bester, M., Głowa, Sibiński, M., Cholewa, M.: Simulation of $TiO_2$/CuO solar cells with SCAPS-1D software. Mater. Res. Express **6**(8), 085918 (2019). https://doi.org/10.1088/2053-1591/ab22aa

Schafer, S., Brendel, R.: Accurate calculation of the absorptance enhances efficiency limit of crystalline silicon solar cells with lambertian light trapping. IEEE J. Photovolt. **8**(4), 1156–1158 (2018). https://doi.org/10.1109/JPHOTOV.2018.2824024

Shen, H., Omelchenko, S.T., Jacobs, D.A., Yalamanchili, S., Wan, Y., Yan, D., Phang, P., Duong, T., Wu, Y., Yin, Y., Samundsett, C., Peng, J., Wu, N., White, T.P., Andersson, G.G., Lewis, N.S., Catchpole, K.R.: In situ recombination junction between p-Si and $TiO_2$ enables high-efficiency monolithic perovskite/Si tandem cells. Sci. Adv. **4**(12), eaau9711 (2018). https://doi.org/10.1126/sciadv.aau9711

Shockley, W., Queisser, H.J.: Detailed balance limit of efficiency of p-n junction solar cells. J. Appl. Phys. **32**(3), 510–519 (1961). https://doi.org/10.1063/1.1736034

Singh, R., Singh, P.K., Bhattacharya, B., Rhee, H.W.: Review of current progress in inorganic hole-transport materials for perovskite solar cells. Appl. Mater. Today **14**, 175–200 (2019). https://doi.org/10.1016/j.apmt.2018.12.011

Soucase, B.M., Pradas, I.G., Adhikari, K.R.: Numerical simulations on perovskite photovoltaic devices. In: Pan, L., Zhu, G. (eds.) Perovskite Materials: Synthesis, Characterisation, Properties, and Applications 445 (2016). https://doi.org/10.5772/61751

Suemasu, T., Usami, N.: Exploring the potential of semiconducting $BaSi_2$ for thin-film solar cell applications. J. Phys. D Appl. Phys. **50**(2), 023001 (2017). https://doi.org/10.1088/1361-6463/50/2/023001

Takabe, R., Hara, K.O., Baba, M., Du, W., Shimada, N., Toko, K., Usami, N., Suemasu, T.: Influence of grain size and surface condition on minority-carrier lifetime in undoped n-$BaSi_2$ on Si(111). J. Appl. Phys. **115**, 193510 (2014). https://doi.org/10.1063/1.4878159

Takahashi, K., Nakagawa, Y., Hara, K.O., Kurokawa, Y., Usami, N.: Investigation of p-type emitter layer materials for heterojunction barium disilicide thin film solar cells. Jpn. J. Appl. Phys. **56**(5S1), 05DB04 (2017). https://doi.org/10.7567/JJAP.56.05DB04

Tian, Y., Vismara, R., Van Doorene, S., Šutta, P., Vančo, L., Veselý, M., Vogrinčič, P., Isabella, O., Zeman, M.: Oxidation-induced structure transformation: thin-film synthesis and interface investigations of barium disilicide toward potential photovoltaic applications. ACS Appl. Energy Materials **1**(7), 3267–3276 (2018). https://doi.org/10.1021/acsaem.8b00486

Tian, Y., Bento-Montes, A.R., Vančo, L., Čaplovičová, M., Vogrinčič, P., Šutta, P., Satrapinskyy, L., Zeman, M., Isabella, O.: Toward $BaSi_2$/Si heterojunction thin-film solar cells: insights into heterointerface investigation, barium depletion, and silicide-mediated silicon crystallization. Adv. Mater. Interfaces **7**(19), 2000887 (2020). https://doi.org/10.1002/admi.202000887

Tianguo, D.: Carrier transport properties in $BaSi_2$ and structure design of $BaSi_2$ solar cells, PhD diss., University of Tsukuba. (2019)

Toh, K., Saito, T., Suemasu, T.: Optical absorption properties of $BaSi_2$ epitaxial films grown on a transparent silicon-on-insulator substrate using molecular beam epitaxy. Jpn. J. Appl. Phys. **50**(6R), 068001 (2011). https://doi.org/10.1143/JJAP.50.068001

Vismara, R., Isabella, O., Zeman, M.: Organometallic halide perovskite/barium di-silicide thin-film double-junction solar cells. Photon. Sol. Energy Syst. **9898**, 54-62 (2016). https://doi.org/10.1117/12.2227174

Wang, L., He, J., Shang, X., Li, M., Yu, Y., Zha, G., Ni, H., Niu, Z.: Enhanced tunneling in the GaAs $p^+$-$n^+$ junction by embedding InAs quantum dots. Semicond. Sci. Technol. **27**(11),115010 (2012). https://doi.org/10.1088/0268-1242/27/11/115010

Wang, Z., Song, Z., Yan, Y., Liu, S., Yang, D.: Perovskite: a perfect top cell for tandem devices to break the S-Q Limit. Adv. Sci. **6**(7), 1801704 (2019). https://doi.org/10.1002/advs.201801704

Werner, J., Niesen, B., Ballif, C.: Perovskite/silicon tandem solar cells: marriage of convenience or true love story? An overview. Adv. Mater. Interfaces **5**(1), 1700731 (2018). https://doi.org/10.1002/admi.201700731

Yachi, S., Takabe, R., Toko, K., Suemasu, T.: Effect of p-$BaSi_2$ layer thickness on the solar cell performance of p-$BaSi_2$/n-Si heterojunction solar cells. Jpn. J. Appl. Phys. **56**(5S1), 05DB03 (2017). https://doi.org/10.7567/JJAP.56.05DB03

Zhang, C., Gwamuri, J., Andrews, R., Pearce, J.M.: Design of multijunction photovoltaic cells optimized for varied atmospheric conditions. Int. J. Photoenergy **2014**, 1–7 (2014). https://doi.org/10.1155/2014/514962